Coherent Betatron Oscillation (CBO) Systematic Study Status Report

Eric F. Schmidt[1,2] and William M. Morse[1]

[1]Physics Department, Brookhaven National Laboratory, Upton, NY 11973
[2]Science Undergraduate Laboratory Internships (SULI); email: schmide2@my.erau.edu

December 12, 2016

Abstract

The E821 experiment made the simplifying assumption that the detector acceptance was linearly dependent on the muon position at the time of decay. Since the acceptance as a function of position can be expanded in a power series, only up to the first-order term was used. However, in E989 an increase in precision is needed so the linear dependence assumption is no longer sufficient. This project aimed to determine if the number of detections has a higher-order dependence on the muons' x-positions at the time of decay while studying various relationships between positrons and gammas that contacted the calorimeters. In this work, the dependence was studied analytically for a generic beam shape and numerically for multiple beam shapes, then compared to particle tracking results. Current results show that there is a quadratic influence of about 10%, which is neither a large influence nor is it negligible, indicating that ART is required for higher-precision.

1 Introduction

The basic physics equation to describe the rate of detected positrons is [1]

$$\frac{dN(t; E_{th})}{dt} = N_0 e^{-t/\gamma\tau_\mu}[1 + A\cos(\omega_a t + \phi)] \tag{1}$$

where E_{th} is the energy threshold, N_0 is the normalization, A is the asymmetry, and ϕ is the initial phase. The fit was modified for E821 to account for the coherent betatron oscillation (CBO) of the muon beam:

$$N_0 \to N_0 \left[1 + A_N e^{-t/\tau_{CBO}}\cos(\omega_{CBO}t + \phi_N)\right] \tag{2}$$

$$A \to A \left[1 + A_A e^{-t/\tau_{CBO}}\cos(\omega_{CBO}t + \phi_A)\right] \tag{3}$$

$$\phi \to \phi + A_\phi e^{-t/\tau_{CBO}}\cos(\omega_{CBO}t + \phi_\phi) \tag{4}$$

Here we will study N_0 (Eq. 2). For clarity and simplicity, N_0 will be referred to as N_D and ω_{CBO} will simply be ω. The section of Eq. 2 inside the brackets will be referenced as the acceptance, A_D. Generally, the detector acceptance is a function of x, x', y, y', S_x, etc... We study the x dependence in this note. A_D can be expanded in a power series:

$$A_D(x) = k_0 + k_1 x + k_2 x^2 + ... \tag{5}$$

where k_i are constants. In E821 only the first two terms were used, here we will add in the quadratic term. Note that Eq. 2 is a function of time and Eq. 5 is a function of x, in reality the position x is a function of the average particle position $\bar{x} = \bar{x}(t)$ and the beam width $\sigma = \sigma(t)$.

1

We are assuming that $\bar{x}(t)$ and $\sigma(t)$ can each be expanded into a Fourier series:

$$\bar{x}(t) = x_0 + \sum_{N=1}^{\infty} f_{\bar{x}N}(t) A_{\bar{x}N} \cos(\omega N t + \phi_{\bar{x}N})$$

$$\sigma(t) = \sigma_0 + \sum_{N=1}^{\infty} f_{\sigma N}(t) A_{\sigma N} \cos(\omega N t + \phi_{\sigma N})$$

We will only analyze the first ω term in these series as seen in Eqs. 6, 7

$$\bar{x}(t) = x_0 + f_{\bar{x}}(t) A_x \cos(\omega t + \phi_x) \tag{6}$$

$$\sigma(t) = \sigma_0 + f_{\sigma}(t) A_{\sigma} \cos(\omega t + \phi_{\sigma}) \tag{7}$$

where A_x, A_{σ} are constants and $\sigma_0 \geq A_{\sigma}$. $f_{\bar{x}}(t), f_{\sigma}(t)$ are functions that will be provided by the beam dynamics group. A current version can be found in Ref. [2].

Combining $g(x)$ (the particle distribution function for the beam) with Eq. 5, we can state the general form of the equation used to find N_D (the number of particles detected) as

$$N_D(t) = \int g(x) A_D(x) \, \mathrm{d}x. \tag{8}$$

Although $N_D(t)$ does not show an explicit time dependence in the above equation, after integrating and substituting in Eqs. 6 and 7, there will be an explicit time dependence.

1.1 Storage Ring Introduction

In section 4, we will look at particle tracking through the storage ring where positrons created from the muon decay are tracked and investigated. There is a near-constant magnetic field through the beam line around the entire ring set so that the muons travel in a circle when they are at a momentum of 3.094 GeV/c. The positrons have less momentum and therefore are more strongly accelerated by the magnetic field so they arc inward towards the center of the ring. As they travel, many of them pass through various materials, such as the electrodes, or other parts of the ring before possibly contacting a calorimeter (Fig. 1. This interaction can lead to gamma production via Bremsstrahlung and subsequent pair-production from the high-energy gammas as they pass through the matter.

2 Analytic Analysis

2.1 Constant Term in Eq. 5

If we set $A_D(x) = k_0$ we can integrate Eq. 8 to get simply

$$N_D(t) = k_0 N_e \tag{9}$$

where N_e is the total number of positrons. Taking the Fourier transform clearly gives no frequencies.

2.2 Linear Term

If we set $A_D(x) = k_1 x$ we can integrate Eq. 8 to get

$$N_D(t) = k_1 N_e \bar{x} = k_1 N_e (x_0 + f_{\bar{x}}(t) A_x \cos(\omega t + \phi_x)). \tag{10}$$

where $\bar{x}$ is from Eq. 6. We can expand this and get a constant term and a $\cos(\omega t + \phi_x)$ term. Applying the Fourier transform gives us a single frequency at $f = \omega/2\pi$. It should also be noted that there is no dependence on σ.
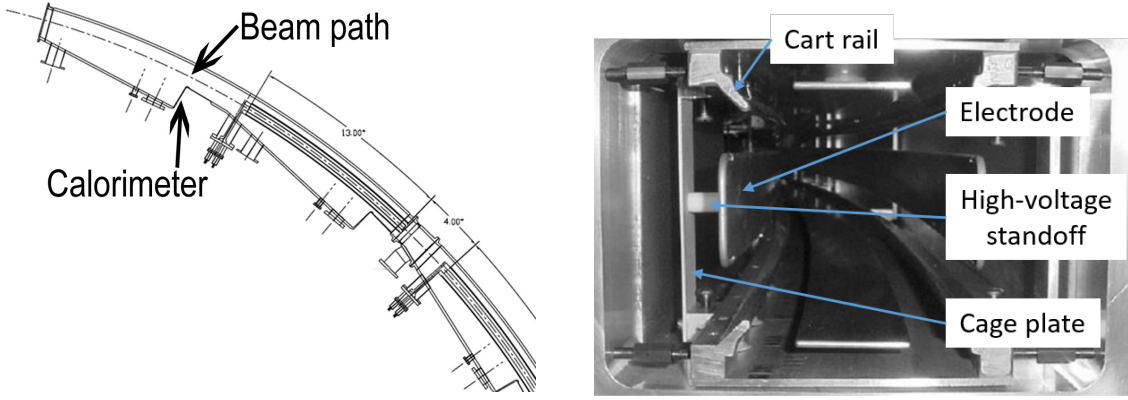
(a) Single section of the muon storage ring showing the optimal beam path and the calorimeters. The calorimeters repeat like this around the entire ring giving a total of 24. Image courtesy of "The Brookhaven muon (g-2) storage ring high voltage quadrupoles" [3].

(b) Looking through a quadrupole, shown as solid lines parallel to and on both sides of the beam path in Fig. 1a. The labeled elements are those that the positrons and gammas can pass through.

Figure 1: Section of muon storage ring and relevant internal parts.

2.3 Quadratic Term

If we set $A_D(x) = k_2 x^2$ we can integrate Eq. 8 to get

$$N_D(t) = \frac{1}{20}k_3 N_e \sigma^2 + k_3 N_e \bar{x}^2 \tag{11}$$

From this we can get a complete equation for N_D

$$N_D(t) = N_e[k_0 + k_1\bar{x} + k_2(\bar{x}^2 + \frac{1}{20}\sigma^2)] \tag{12}$$

substituting in Eqs. 6 and 7 gives

$$N_D(t) = \frac{1}{20}k_3 N_e \sigma_0^2 + k_3 N_e x_0^2 + \frac{1}{10}k_3 N_e \sigma_0 \cos(\omega t + \phi_\sigma) + \frac{1}{20}k_3 N_e \cos^2(\omega t + \phi_\sigma) +$$
$$2k_3 N_e x_0 \cos(\omega t + \phi_x) + k_3 N_e \cos^2(\omega t + \phi_x) \tag{13}$$

that we can simplify by folding multiple constant coefficients into single constants and transforming the $\cos^2()$ into something more useful.

$$N_D(t) = N_e[(A_0 x_0^2 + A_1 \sigma_0^2) + B_0 f_x(t)\cos(\omega t + \phi_x) + B_1 f_\sigma(t)\cos(\omega t + \phi_\sigma) +$$
$$C_0(f_x(t))^2\cos(2\omega t + \phi_x) + C_1(f_\sigma(t))^2\cos(2\omega t + \phi_\sigma)]. \tag{14}$$

When we take the Fourier transform of Eq. 14, ϕ_x, ϕ_σ become constant coefficients and therefore do not affect the frequencies. After the transform we get frequencies $f = \omega/2\pi, f = 2(\omega/2\pi)$.

Although the frequencies found here are in agreement with a prior analytical analysis [?], this note finds a different final equation. The reason for this is that the previous analysis done assumed equations for $\bar{x}$ and σ of

$$\bar{x} = x_0 f(t)[1 + A_{\bar{x}}\cos(\omega t)]$$

$$\sigma = \sigma_0 f(t)[1 + A_\sigma \cos(\omega t)]$$

which has the decoherence function $f(t)$ attached to the x_0 and σ_0 terms, where in this note, they are not attached (Eq. 6, 7).

3 Numeric Analysis

Here we will study three different beam shape functions, a constant particle distribution, a quadratic, and a Gaussian. Studying multiple distributions is done because the actual beam shape is not a perfectly fit distribution but some combination of them. The constants k_0, k_1, k_2 used below in the acceptance function A_D were found from fitting the tracking data in section 4, "Muon Decay Tracking". We will be skipping the analysis of the constant acceptance term from Eq. 5.

Note: It's important to keep in mind that the constants k_i used below will change as more data is taken and assumptions are removed as discussed in section 4.

3.1 Constant Distribution

Let's start by studying a constant particle distribution function

$$g(x) = p. \tag{15}$$

where p is some constant.

Linear Term from the Expansion (Eq. 5) Using the linear acceptance function, $A_D(x) = k_0 + k_1 x$, and combining it with our constant distribution function, we can get a function for N_D

$$N_D(t) = \int a\, p\, (k_0 + k_1 x)\, \mathrm{d}x \tag{16}$$

where a is a normalizing factor to ensure the total number of particles doesn't change with each step in the numerical integration process. Integrating numerically and taking the Fourier transform we get Fig. 2. We can see that changing the beam width σ does not have an effect on the acceptance, unlike changing the beam position $\bar{x}$. The frequency is about $f \approx 0.6$ MHz. The CBO found from beam structure plots [4] was about $(6\pi/5) \times 10^6$ rad/s. Therefore the final acceptance containing a $\cos(\omega t)$ term, with no higher-order terms, should give a frequency of $f \approx 3/5$ MHz, which is what we have found.

Quadratic Term from the Expansion Now Let's assume A_D depends quadratically on position giving us the general function

$$A_D = k_0 + k_1 + k_2 x^2 \tag{17}$$

which allows us to set up the new function for N_D:

$$N_D(t) = \int a\, p(k_0 + k_1 + k_2 x^2)\, \mathrm{d}x \tag{18}$$

which, after integrating and taking the Fourier transform, provides us with Fig. 3 where we get 2 frequencies. The frequencies found are at $f_1 \approx 0.6$ MHz, $f_2 \approx 1.2$ MHz. These are in line with the acceptance function containing a $\cos(\omega t)$ term and a $\cos(2\omega t)$ term, with no higher-order terms. We can also see that the amplitude of the 2nd-order cosine term is much smaller than the 1st-order term. This indicates that even if a quadratic dependence exists, it should be much smaller than the linear dependence.
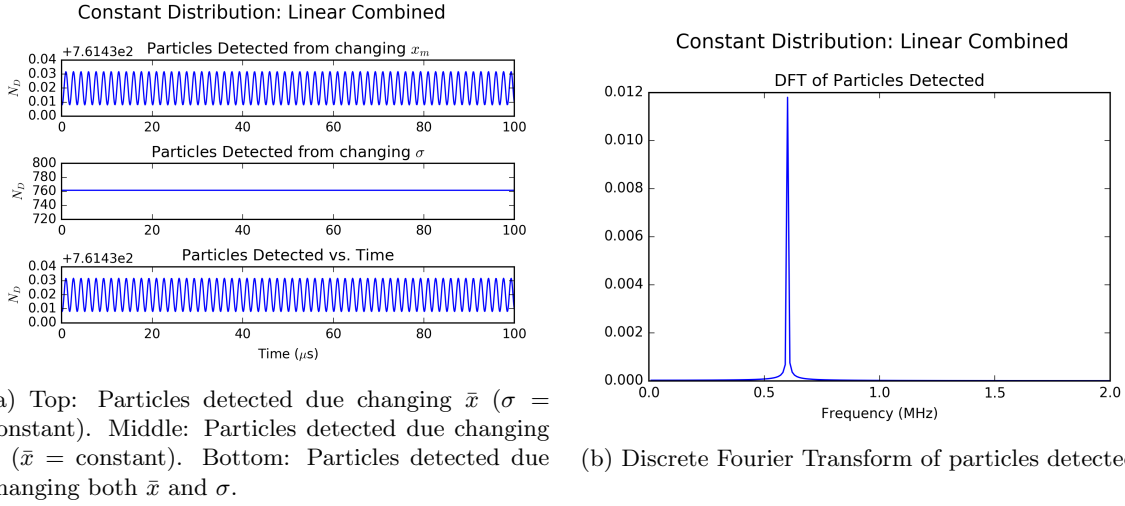
(a) Top: Particles detected due changing $\bar{x}$ (σ = constant). Middle: Particles detected due changing σ ($\bar{x}$ = constant). Bottom: Particles detected due changing both $\bar{x}$ and σ.

(b) Discrete Fourier Transform of particles detected.

Figure 2: Constant distribution, linear term

(a) Top: Particles detected due changing $\bar{x}$ (σ = constant). Middle: Particles detected due changing σ ($\bar{x}$ = constant). Bottom: Particles detected due changing both $\bar{x}$ and σ.

(b) Discrete Fourier Transform of particles detected. The constant k_2 was multiplied by 100 for this plot to show where the second frequency resides (not distinguishable with the actual value of k_0)
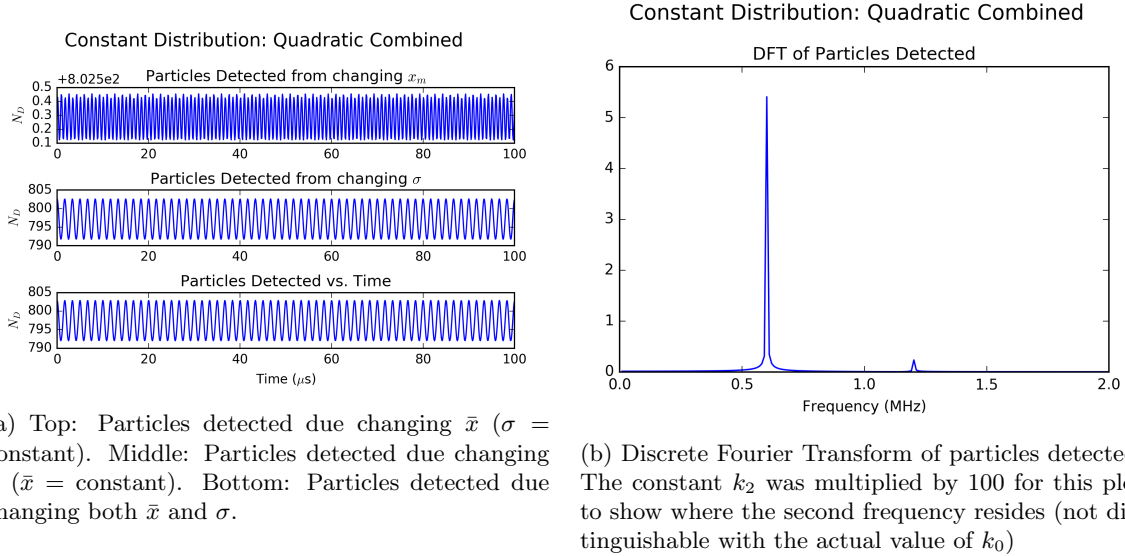
Figure 3: Constant distribution, quadratic term

3.2 Quadratic Distribution

Now let's study the situation where the beam has a quadratic distribution

$$g(x) = a(x - \bar{x})^2 + b \tag{19}$$

where $\bar{x}$ is the optimal beam path location described by Eq. 6, and a and b depend on σ (Eq. 7), the beam distribution width, and are renormalized with each step through time so that when the function is integrated over x, we get the correct number of particles. We will look at this distribution in the exact same way as the linear distribution above.

Linear Term from the Expansion Equation (Eq. 5) Let's assume A_D depends linearly on position giving us

$$A_D = k_0 + k_1 x \tag{20}$$

Plugging Eqs. 20 and 19 into Eq. 8 gives us an equation to find N_D

$$N_D = \int (a(x - \bar{x})^2 + b)(k_0 + k_1 x) \, \mathrm{d}x \tag{21}$$

where a and b are updated each step in the integration process to ensure the total number of particles remains constant. Once again, we numerically integrate the above equation and get results found in Fig. 4. As with the linear distribution function, we get no change in the acceptance due to a change in the beam width and only one frequency, $f \approx 0.6$ MHz, from changing the beam center location.
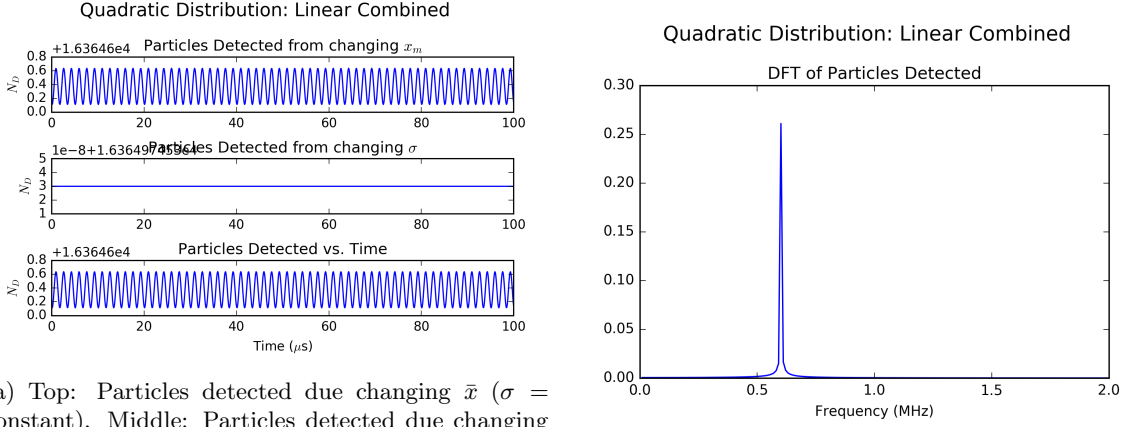
(a) Top: Particles detected due changing $\bar{x}$ ($\sigma =$ constant). Middle: Particles detected due changing σ ($\bar{x} =$ constant). Bottom: Particles detected due changing both $\bar{x}$ and σ.

(b) Discrete Fourier Transform of particles detected.

Figure 4: Quadratic distribution, linear term

Quadratic Term from the Expansion We will use the same equation for acceptance as we did above in Eq. 17. We can now form our equation to find N_D,

$$N_D = \int \left[(a(x - \bar{x})^2 + b) \left(k_0 + k_1 x + k_2 x^2 \right) \right] \, \mathrm{d}x \tag{22}$$

that we can integrate and take the Fourier transform of to get Fig. 5. We see the same results as we did for the quadratic term with the constant distribution above: $f_1 \approx 0.6$ MHz, $f_2 \approx 1.2$ MHz and the magnitude of $f_1 \gg f_2$. Note that the magnitudes of the frequencies found can vary slightly depending on the values of the constants entered into Eq. 22 (however the frequencies themselves don't change).

3.3 Gaussian Distribution

Now let's study the situation where the beam has a Gaussian distribution

$$g(x) = a \cdot \frac{1}{\sqrt{2\pi\sigma^2}} e^{-\frac{(x - \bar{x})^2}{2\sigma^2}} \tag{23}$$

where a is the normalization constant to keep the correct number of particles in the beam. We will look at this distribution in the exact same way as the other two distributions above.
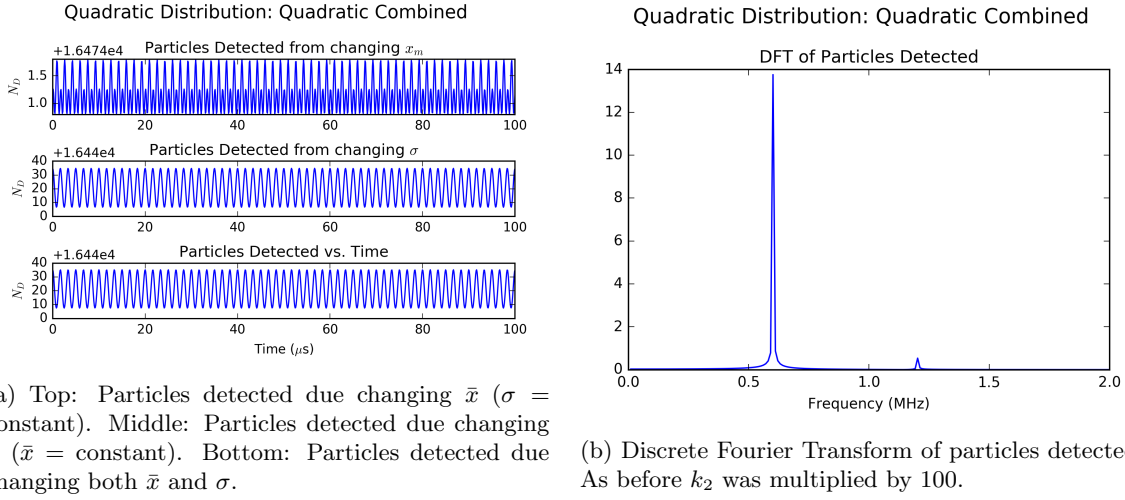
(a) Top: Particles detected due changing $\bar{x}$ ($\sigma =$ constant). Middle: Particles detected due changing σ ($\bar{x} =$ constant). Bottom: Particles detected due changing both $\bar{x}$ and σ.

(b) Discrete Fourier Transform of particles detected. As before k_2 was multiplied by 100.

Figure 5: Quadratic distribution, quadratic term

Linear Term from the Expansion   As before, we can set up the equation for N_D as

$$N_D = \int g(x)(k_0 + k_1 x) \, \mathrm{d}x \tag{24}$$

that we integrate and find the Fourier transform of to get the results in Fig. 7. Once again, as with the other two beam shapes, we see only a single frequency at $f \approx 0.6$ MHz.
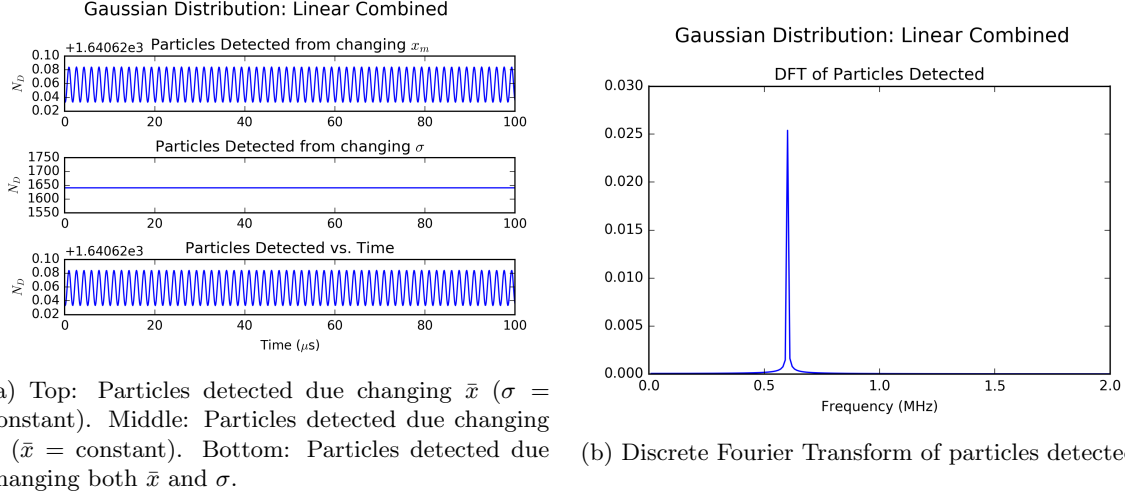

(a) Top: Particles detected due changing $\bar{x}$ ($\sigma =$ constant). Middle: Particles detected due changing σ ($\bar{x} =$ constant). Bottom: Particles detected due changing both $\bar{x}$ and σ.

(b) Discrete Fourier Transform of particles detected.

Figure 6: Quadratic distribution, quadratic term

Quadratic Term from the Expansion   The last situation we are studying here is that of the Gaussian distribution with a quadratic dependence. We can form our equation to find N_D,

$$N_D = \int g(x)(k_0 + k_1 x + k_2 x^2) \, \mathrm{d}x \tag{25}$$

which gives us Fig. 7. Here we see something new, in addition to the two frequencies $f_1 \approx 0.6$ MHz and $f_2 \approx 1.2$ MHz that we've seen before, we also get others at $f_n \approx 0.6$ MHz $* n$ where n is a positive

integer. The possible values of n are not fully known as the amplitude of the frequency decreases rapidly with increasing n so only $n = 3$ can easily be seen on the plot here but more can be found upon further examination. There are two mentionable concepts relating to these extra frequencies:

1. It is currently unclear if the extra frequencies represent real physical phenomena or not. It is possible they are due to mathematical inaccuracies that arise from the edges of the Gaussian function being cut off (the actual beam shape does not have infinite tails as the Gaussian function represents it as having), coupled with the non-linear nature of the quadratic dependence. When this was investigated analytically, no solution was found when attempting to take the Fourier transform of Eq. 25. In contrast, analytical results for all other beam shapes gave results equal to the numerical results shown here.

2. The amplitudes of the frequencies with $n > 1$ are very small, especially so at $n > 2$. Even if they represent a real physical phenomenon, their influence is incredibly small.
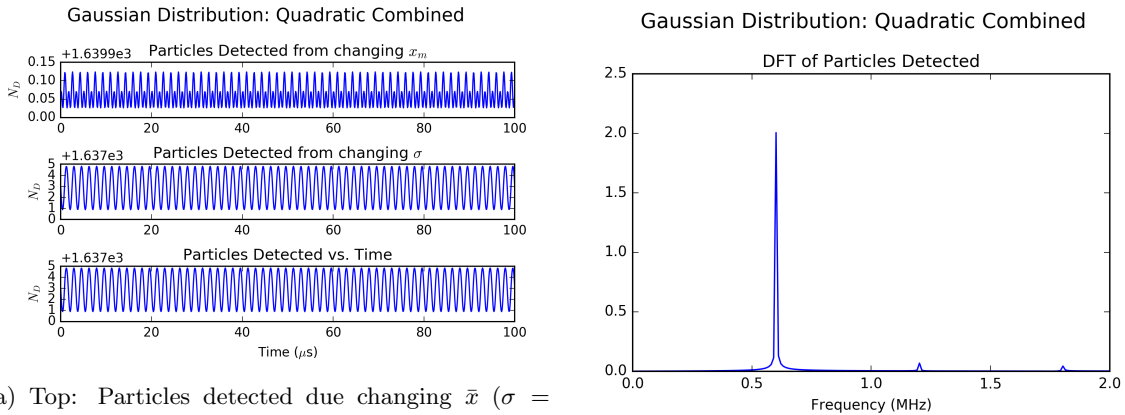
(a) Top: Particles detected due changing $\bar{x}$ ($\sigma = $ constant). Middle: Particles detected due changing σ ($\bar{x}$ = constant). Bottom: Particles detected due changing both $\bar{x}$ and σ.

(b) Discrete Fourier Transform of particles detected. As before, k_2 was multiplied by 100.

Figure 7: Quadratic distribution, quadratic term

4   Muon Decay Tracking

4.1   Methods

Positrons of energies greater than 1.8 GeV [1] created by muon decay were tracked using Python as they curled towards the center of the ring due to the Lorentz force. Sometimes they passed through ring material possibly losing energy due to Bremsstrahlung. They were tracked until they either lost too much energy to be useful (< 0.2 GeV) or were 'killed' by either hitting the calorimeter (front or edge) or entering the inner part of the ring. In addition to Bremsstrahlung, pair-production events were taken into consideration and their by-products were also tracked. The muon phase-space data that provided the all possible positron initial conditions at the time of the muon decay can be seen in Appendix A.

The muon data set used (provided by D. Rubin) has 5171 muons taken at 100 μs after injection, however, to get lower statistical uncertainties, and allowed by the randomness involved in the decay process, this data set was used almost 8 times to get a total of 44732 initial positrons.

4.1.1   Simplifying Assumptions

Some simplifying assumptions were made, which are discussed here. In time, these will be removed.

8

Electric and Magnetic Fields   The electric field is assumed to only exist inside the quads and the magnetic field is assumed to be constant everywhere. In reality, there is a non-zero electric field outside the quads and the magnetic field weakens and takes on a non-zero radial field.

Bremsstrahlung   The gamma momentum vector released via Bremsstrahlung was assumed to be parallel to the particle momentum vector [5].

Compton Scattering   Due to the high-energy of the gammas produced from Bremsstrahlung, Compton scattering was ignored [6].

Ring Geometries   Two of the storage ring structures, high-voltage standoffs and standoff plates, were geometrically approximated by allowing them to 'bend' radially around the ring (to greatly simplify their coding). However, due to their small sizes, this approximation causes deviations of only small fractions of a millimeter from their true shapes. In addition, the curls at the edges of the electrodes were not added as their geometries are complicated to code. This assumption is acceptable as the curls are very small compared to the size of the electrodes themselves.

Trolley Rails   Due to the odd shape (being very difficult to represent digitally) and relatively large thickness, it was assumed that if any particle or gamma made contact with a trolley rail, the particle or gamma would no longer be tracked, i.e. it was 'killed'. This is a valid assumption because 1) the rails were large enough to cause a very large reduction in energy of the particle passing through them (preventing them from contacting the calorimeter), and 2) only about 0.2% of particles make contact with them.

4.2   Results

Table 1 gives the aggregate results of the tracked positrons and gammas, table 2 gives the particle tracking results, and table 3 gives the photon tracking results.

Table 1: 43888 total muon decays were tracked (about 8.5 repeat uses of the muon data set). The average contact angle the particles made with the calorimeters was ≈ 82 deg. The average contact angle the gammas made with the calorimeters was ≈ 87.7 deg.

| Total # of Tracked Positrons	Total # of Bremsstrahlung Events	Total # of Pair-Production Events	Total # of Calorimeter Hits by Positrons	Total # of Calorimeter Hits by Gammas
44310	9510	422	34328 ($\approx 77\%$)	998 ($\approx 10\%$)

Table 2: Table gives the number of positrons that contacted a certain element, some positrons contacted more than one element.

Location	Positron Contacts	% of Total Contacts	% of Total Positrons	Gammas Created	% of Total Gammas
Quad Electrode	15936	68%	36%	5999	63%
Cage Plate	3671	16%	8%	2290	24%
HV Standoff	2048	9%	5%	868	9%
HV Standoff Screw	471	2%	1%	353	4%
Trolley Rail	1293	5%	3%	N/A	N/A
Total	34328	100%	77%	9510	100%

Table 3: Tables gives the number of pair-production events by location. 998 out of 9510 total gammas contacted the calorimeter ($\approx 10\%$).

Location	Pair-Production Events	% of Total P.P. Events	% of Total Gammas
Electrodes	290	69%	3%
Cage Plates	80	19%	0.8%
HV Standoffs	34	8%	0.4%
HV Standoff Screws	18	4%	0.2%
Total	422	100%	4.5%

Fig. 8 gives the results of the position on the calorimeter where the particles and photons made contact. Fig. 10a samples 10 positrons and their associated gammas and plots them together on the calorimeter front surface, showing their separation. Fig. 10b shows how the gamma energy affects the distance on the front calorimeter between it and its parent positron. There is no significant correlation between the energy of the gamma produced and its separation distance from its parent positron on the calorimeter.
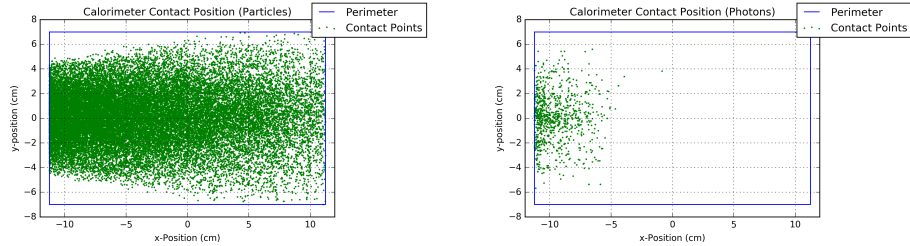
(a) Position on the calorimeter where the particles made contact. The blue rectangle represents the edge of the calorimeter.

(b) Position on the calorimeter where the photons made contact. The blue rectangle represents the edge of the calorimeter.

Figure 8: Calorimeter contact data for the positrons.
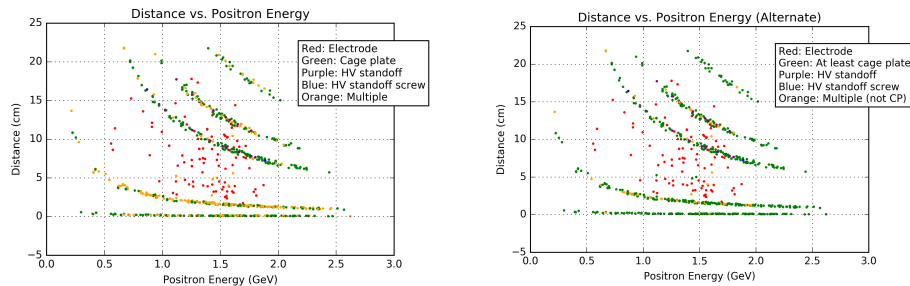
(a) A plot showing the distance between positron/gamma pair contact points on the front of the calorimeter as a function of the positron momentum at the time of calorimeter contact.

(b) This plot shows the dominance of the cage plate. The green points now include positrons that passed through the cage plate and possibly another element and the orange now is only for those that passed through multiple elements but not the cage plate.

Figure 9: Calorimeter contact data for positrons and gammas they created if both the positron and the gamma contacted the front of the calorimeter (referred to as a positron/gamma pair).
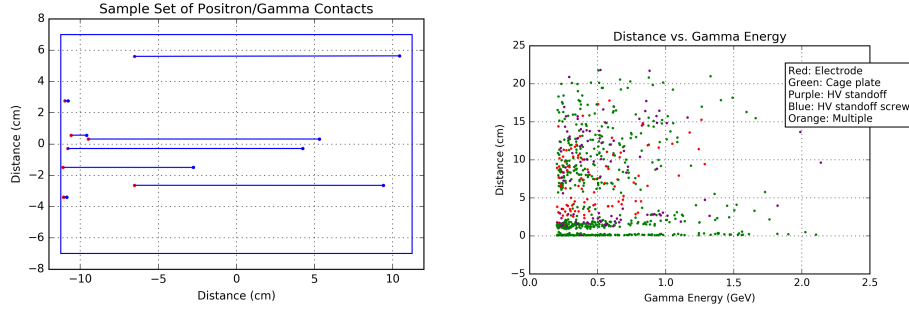
(a) Sample set of positrons that contacted the calorimeter front and also created a gamma that contacted the calorimeter front. Gammas are red, positrons are blue, and the blue line connects the elements in each pair.

(b) Plot of distance on the calorimeter front between a positron and its associated gamma in the positron/gamma pair as a function of the gamma energy.

Figure 10: Calorimeter contact data for positrons and gammas they created.

Fig. 11 shows the energy distributions of all the created gammas and those that contacted the calorimeter. The energy allowed during Bremsstrahlung was > 0.04 GeV but only those > 0.2 GeV were tracked. This is primarily because below 0.2 GeV, Compton scattering becomes non-negligible [7] and Compton scattering is currently not an included effect in the tracking. In addition, it already requires 9 gammas and particles of 0.2 GeV combined to reach the 1.8 GeV threshold.
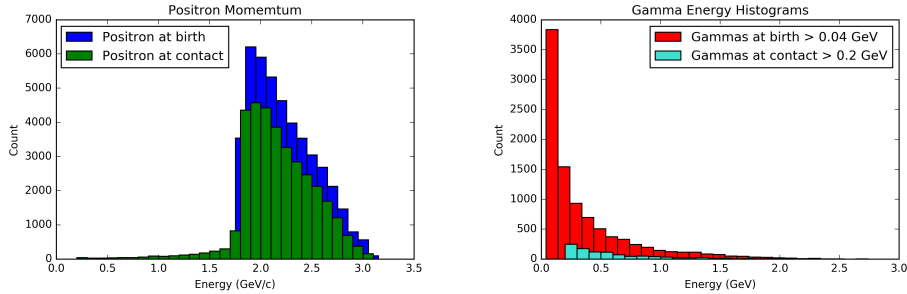
(a) Momentum distributions of the positrons. Only 'muon decayed' positrons are shown, pair-produced positrons are not included here. 'Concact' refers to those that contacted the calorimeter.

(b) Energy distributions of the photons. Photon energy > 0.04 GeV was allowed during Bremsstralung but only those above 0.2 GeV were tracked. 'Concact' refers to those that contacted the calorimeter.

Figure 11: Energy and momentum distributions for gammas and positrons both at birth and for those that contacted the calorimeter.

The calorimeter acceptance was then calculated and plotted. This was done by first splitting the positrons into 2 parts, those that passed through an electrode and those that did not. Next, each of the two sections was further split by the starting x-position range into 8 sections of 1 cm each then for each section, applying the following formula to find the acceptance A:

$$A = \frac{D}{N} \tag{26}$$

where D is the number of detected particles for that section and N is the total number of particles that also started in that 1 cm wide section and that either passed through or missed the electrodes, depending on what is being plotted. Fig. 12 shows the results.
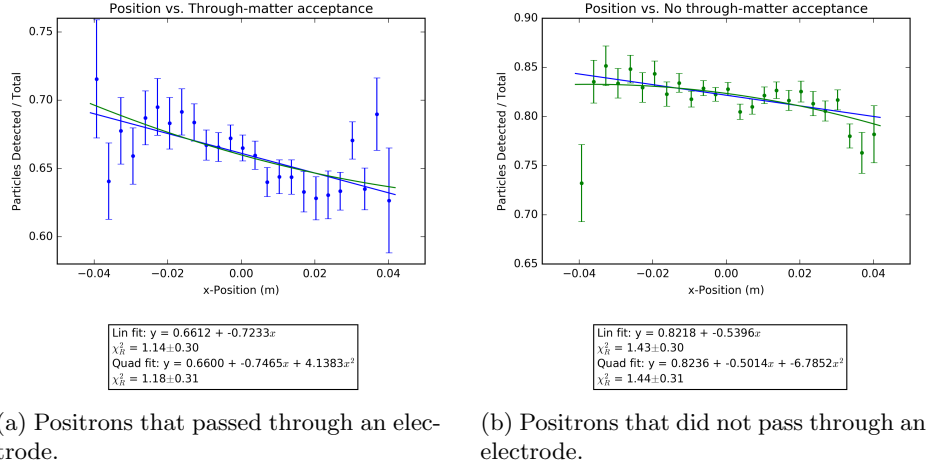

(a) Positrons that passed through an electrode.

(b) Positrons that did not pass through an electrode.

Figure 12: Acceptance for each 1 cm section where 'Total' in the y-axis refers to the total number of muons inside the 1 cm wide section at the time of decay.

We can see that the acceptance is currently consistent with linear. As assumptions are removed from the study and more data is studied, a larger quadratic dependency may be found.

5 Combining Results

We now need to combine the fitting functions we found in the tracking section with the solutions for both linear and quadratic expansion terms found from our analytic investigation. To do this we will take the constants for linear and quadratic fits for the acceptance vs. position plots in Fig. 12 and insert them into the equation for N_D (Eq. 12). The values of $\bar{x} \approx 0.45$ mm and $\sigma \approx 2.9$ mm come 30 μs after injection (data provided by David Rubin [2]).

Table 4 gives the influence of the quadratic term as it relates to both those positrons that pass through matter or avoid all matter entirely. If positrons do not pass through matter, there is no real quadratic influence, the acceptance is linearly dependent on the the x-position of the muon at decay. On the other hand, there seems to be a non-negligible quadratic influence on the acceptance of those particles that pass through matter. More data is required to refine and substantiate these findings.

Table 4: Results giving the influence of the quadratic term on the acceptance for positrons that pass through matter.

Through Matter (Fig. 12a)			Not Through Matter (Fig. 12b)		
Linear Fit	Quadratic Fit	Quadratic Influence	Linear Fit	Quadratic Fit	Quadratic Influence
$0.609N_e$	$0.660N_e$	7.7%	$0.822N_e$	$0.823N_e$	0.22%

6 Conclusion

This note investigated the possibility of a quadratic term in the positron acceptance (detection rate) as a function of muon x-position at the time of muon decay and the influence that it could have. This is

part of a larger investigation into the effect of the coherent betatron oscillation (CBO) on the statistical uncertainties in the system.

Numerically we studied three beam shape functions, constant, quadratic, and Gaussian. We can see that although a second (or possibly more in the case of a Gaussian beam shape) frequency in the acceptance does exist, the amplitude of that frequency is very small compared to the primary frequency.

Next, through particle tracking, the acceptance was found as a function of muon x-position at the time of decay. Although more data is needed, in addition to the removal of some simplifying assumptions, they acceptance is currently consistent with linear however there does seem to be some quadratic influence in the acceptance of positrons that pass through matter.

When combining the equations found from the analytical analysis with the fit functions found in the tracking, we see that there is very little quadratic influence in the acceptance for positrons that do not pass through any matter, $\approx 0.22\%$, whereas the quadratic influence on those positrons that pass through matter is $\approx 7.7\%$. This tells us that we need more data and higher precision to come to a conclusive result, therefore it must land in the realm of ART.

Future work will include not only removing simplifying assumptions, but determining the acceptance as a function of x-prime, y-position, y-prime, and muon spin. In addition, the asymmetry and phase (Eqs. 3,4) dependence on phase-space position and spin will also be investigated.

A Muon Phase-Space Data

The muon phase-space data was provide by David Rubin of Cornell. Figs. 13, 14 show the muon x, x-prime and y, y-prime phase-spaces and a histogram of the muons' longitudinal momentum.
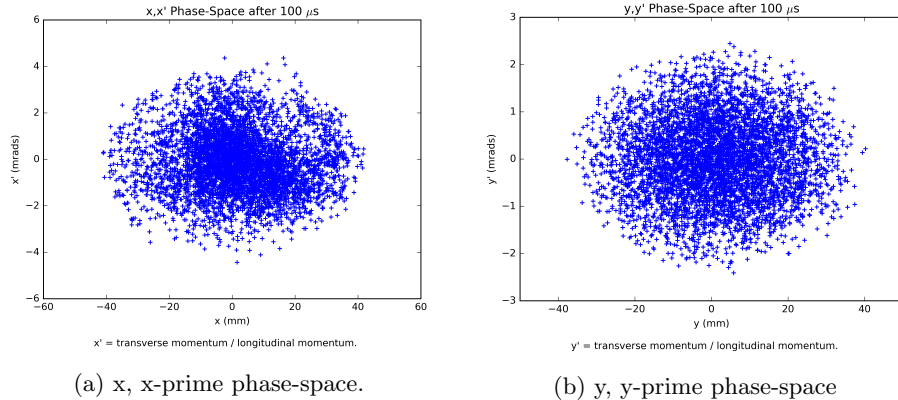

(a) x, x-prime phase-space.

(b) y, y-prime phase-space

Figure 13: Muon phase-space data for stored muons after 100 μs.

References

[1] G. Bennett et al., Phys. Rev. D. 54, 141 (2004)

[2] D. Rubin, E989 Note 86 (2016)

[3] Y.K. Semertzidis et al, Nucl. Instr. Methods A. 503.3 (2003): 458-84.

[4] D. Rubin, DocDB Note 2820 (2015)

[5] Koehn, C., Ebert, U., Atmos. Res. 136, 432 (2014)

[6] NIST XCOM: Element/Compound/Mixture. National Institude of Standards and Technology, n.d. Web. 10 Nov. 2016.
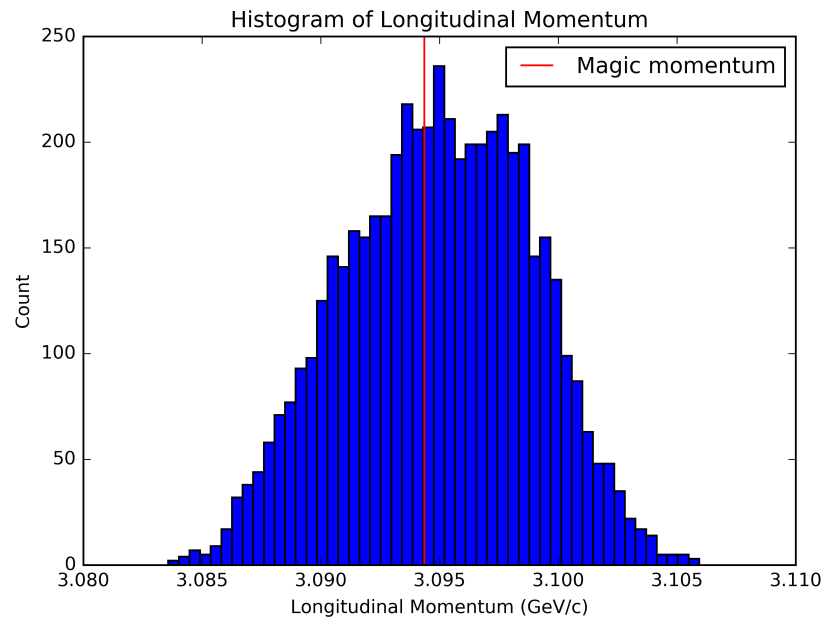
Figure 14: Histogram of the longitudinal muon momentum.

[7] C. Patrignani et al. (Particle Data Group), Chin. Phys. C, 40, 100001 (2016).